Journal of Environmental Chemical Engineering 11 (2023) 109744

Contents lists available at ScienceDirect

Journal of Environmental Chemical Engineering

journal homepage: www.elsevier.com/locate/jece

Metronidazole photodegradation under solar light with UiO-66-NH_2 photocatalyst: Mechanisms, pathway, and toxicity assessment

Y.-L. Wang [a], A. Gómez-Avilés [a], S. Zhang [b], J.J. Rodriguez [a], J. Bedia [a,*], C. Belver [a,*]

[a] Chemical Engineering Department, Universidad Autónoma de Madrid, Campus Cantoblanco, E-28049 Madrid, Spain
[b] State Key Laboratory of Luminescent Materials and Devices, and Guangdong Provincial Key Laboratory of Fiber Laser Materials and Applied Techniques, South China University of Technology, 510641 Guangzhou, China

ARTICLE INFO

Editor: Despo Kassinos

Keywords:
UiO-66-NH_2
Metronidazole
Photodegradation
Pathway
DFT
Toxicity

ABSTRACT

Metronidazole is a nitroimidazole antibiotic that is increasingly detected in aquatic bodies. Therefore, there is an urgent need to research methodologies to remove this and other antibiotics. One of the alternatives is the application of solar photocatalysis, which requires the use of an efficient photocatalyst. In this work, UiO-66-NH_2 was synthesized by a facile solvothermal method and evaluated for the degradation of metronidazole under simulated solar light. The effects of catalyst dosage, initial pH, and metronidazole concentration were discussed, establishing the best operation conditions. In addition, the stability and reproducibility of UiO-66-NH_2 activity were also verified. The quenching reaction showed that holes and superoxide radicals coexisted as the main active species, being responsible for the metronidazole degradation. The pathway of metronidazole photodegradation was proposed by means of density functional theory calculations and LC/ESI-MS analysis. It is noteworthy that this study detected for the first time $C_6H_{11}N_3O_4$, $C_4H_6N_2O_3$, and $C_4H_8N_2O_4$ as metronidazole photodegradation byproducts. ECOSAR toxicity analysis showed that all byproducts were less toxic than the original metronidazole, supporting the potential feasibility of this method for treating water polluted with this antibiotic.

1. Introduction

Antibiotics can be used not only to combat certain infectious diseases in humans but also to promote the growth of poultry and livestock [1,2]. While antibiotics play a positive role, they are also causing problems for human beings and the environment. Antibiotic resistance in pathogenic microorganisms, due to overuse of antibiotics, leads to an increase in the effective doses required to kill bacteria. Low-dose antibiotics are excreted into the environment after they have worked in the body, leading to increased resistance in susceptible bacteria [3]. In addition to causing drug resistance in bacteria, resistance genes may expand and evolve in the environment and may also be toxic to other organisms [4,5]. Metronidazole (MNZ) belongs to the chemical class of nitroimidazole antibiotics, widely used for the treatment and prevention of systemic or local infections caused by sensitive anaerobic bacteria [6–8]. In humans, it is potentially mutagenic and may cause DNA damage and carcinogenicity [9]. The International Agency for Research in Cancer (IARC) also includes metronidazole in its published list of carcinogens [10]. Researchers recently investigated 14 common antibiotics in rivers of 72 countries on six continents and found them in 65% of the monitored sites. In particular, the concentration of metronidazole detected at a location in Bangladesh was 300 times higher than the safe value [11], posing a potential threat to the ecological environment and human health. Therefore, further research on advanced and effective technologies for MNZ removal is necessary.

Advanced oxidation processes (AOPs) have the potential to degrade toxic organic pollutants by completely converting antibiotics into harmless products. These technologies include Fenton oxidation [12], ozone oxidation [13], UV/H_2O_2 [14], persulfate-assisted process [15], and photocatalysis [16–18]. Among them, photocatalysis is a promising technology because light irradiation is more readily available and more cost-effective, especially if solar radiation is used [19,20]. When a semiconductor absorbs photons with sufficient energy, electron-hole pairs are generated that can react directly with the organic pollutants or can trigger the generation of in situ radical species ($^{\bullet}O_2^-$ or $^{\bullet}OH$) capable of oxidizing those contaminants [21,22]. For instance, Tran et al. degraded 50 mg·L^{-1} metronidazole with TiO_2 under UV light achieving removal of 86% in 1 h [23]. Hsieh et al. prepared

* Corresponding authors.
E-mail addresses: jorge.bedia@uam.es (J. Bedia), carolina.belver@uam.es (C. Belver).

https://doi.org/10.1016/j.jece.2023.109744
Received 1 December 2022; Received in revised form 6 March 2023; Accepted 19 March 2023
Available online 21 March 2023

ZnO/graphene quantum dots that were tested as photocatalysts for the degradation of metronidazole, achieving complete MNZ removal after 0.5 h under UV irradiation [24]. However, ultraviolet light accounts for a small percentage of sunlight which means low utilization of solar light. Therefore, looking for photocatalysts responsive to both UV and visible light can help to greatly improve the degradation efficiency.

The open metal sites and light-responsive organic ligands of metal organic frameworks (MOFs) are excellent candidates for solar photocatalysis [25–28]. Zr-based UiO-66-NH_2, as thermally and chemically stable MOFs is an ordered crystalline structure consisting of 2-aminoterephthalate ligands linked to Zr-O clusters [29,30]. The amine group is able to absorb light in the visible region, resulting in better light utilization and photocatalytic performance [31,32]. Herein, we synthesized pristine UiO-66-NH_2 by a solvothermal method [33]. The stability in water and other surface properties (i.e., point of zero charge (pH_{pzc})) were studied first. The photocatalytic performance of UiO-66-NH_2 was tested under simulated solar light for the removal of MNZ in aqueous solutions. Different operation variables (catalyst dosage, solution pH and MNZ concentration) were investigated in detail. A rational photocatalytic mechanism was initially declared based on scavenger experiments and the electrochemical determination of the band structure. The stability and reusability of UiO-66-NH_2 were determined by recycling experiments. Density functional theory calculations (DFT) were used to determine the potential reaction sites located on UiO-66-NH_2. These results were coupled with the experimental analysis of the treated water by mass spectroscopy to propose a novel degradation pathway. The toxicity of the detected products was evaluated for the first time using ECOSAR software.

2. Experimental

2.1. Materials

All reagents were used without further purification and purchased at analytical grade. 2-aminoterephthalic acid (2ATA, $C_8H_7NO_4$, 99%), Zirconium butoxide ($Zr(OC_4H_9)_4$, 80%), metronidazole (MNZ, $C_6H_9N_3O_3$, ≤ 100%), methanol (CH_3OH, ≥99.9%), formic acid (HCOOH, ≥ 95%), triethanolamine (TEA, $C_6H_{15}NO_3$, 99%), 4,5-dihydroxy-1,3-benzenedisulfonic acid disodium salt monohydrate (Tiron) ($C_6H_4Na_2O_8S_2{\cdot}H_2O$, 97%), silver nitrate ($AgNO_3$, ≥ 99%), sodium bicarbonate ($NaHCO_3$, 99.5–100.5%), sodium chloride (NaCl, ≥ 99%) and humic acid were purchased from Sigma-Aldrich company. 2-propanol (C_3H_8O, 99.7%), N,N-dimethylformamide (DMF, C_3H_7NO, ≥ 99.8%) and sodium nitrate ($NaNO_3$, 99%) were supplied by Panreac. Sodium sulfate (Na_2SO_4, 99–101%) was supplied by Scharlau. Stock solutions have been prepared in ultra-purified water obtained from a Milli-Q system.

2.2. Preparation of UiO-66-NH_2

The synthesis of UiO-66-NH_2 was conducted using a previously reported solvothermal approach [33]. Typically, 1.5 mmol of 2ATA, 1.5 mmol of $Zr(OC_4H_9)_4$ and 10 mL of formic acid were dissolved into 20 mL of DMF in a 100 mL Schott bottle, followed by an ultrasonic treatment at room temperature until obtaining a transparent solution. Afterwards, the Schott bottle was sealed and heated at 120 ℃ for 24 h. After cooling to room temperature, the slurry was washed out with DMF and methanol several times by centrifugation. Then, the collected samples were dried at 70 ℃ overnight under a vacuum.

2.3. Photodegradation experiments

The photocatalytic performance of UiO-66-NH_2 was evaluated via the degradation of MNZ under simulated sunlight using a solar simulator with a Xe lamp (Suntest XLS+, ATLAS), fixing the intensity at 600 $W{\cdot}m^{-2}$, and limiting the radiation above 320 nm with a rate constant. In every experiment, the photocatalyst (125 $mg{\cdot}L^{-1}$) was evenly added to 150 mL of MNZ solution (5 $mg{\cdot}L^{-1}$) in the dark for 16 h to establish the adsorption-desorption equilibrium before exposing it to solar irradiation. All experiments were performed at a constant temperature, fixed at 20 °C using a thermostatic bath. At specific time intervals, up to 6 h, 0.45 mL of the aqueous suspension was withdrawn and filtered with a 0.2 μm PTFE syringeless filter for further analysis. Most of the essays were carried out at the natural pH of the MNZ solution, c.a. 6.9. In those cases where pH modification was required, HCl (0.1 M) or NaOH (0.1 M) solutions were used. The impact of natural inorganic anions and humic acid was conducted by amending the initial MNZ solution with Cl^- (25 $mg{\cdot}L^{-1}$), NO_3^- (50 $mg{\cdot}L^{-1}$), SO_4^{2-} (50 $mg{\cdot}L^{-1}$), HCO_3^- (150 $mg{\cdot}L^{-1}$), or humic acid (25 $mg{\cdot}L^{-1}$), which are representative concentrations in actual water bodies [34]. Trapping experiments were carried out following the same conditions, adding the corresponding scavenger to the solution. TEA/$AgNO_3$/Tiron/2-propanol were regarded as quenchers of $h^+/e^-/{}^{\bullet}O_2^-/{}^{\bullet}OH$, respectively, using a 1 mM concentration in all essays. The stability and reusability of UiO-66-NH_2 were evaluated by conducting four successive reaction cycles under simulated solar light. After each cycle, the used photocatalyst was collected by vacuum filtration and dried, then used for the next cycle. The reaction rate of MNZ photodegradation was estimated by the pseudo-first-order kinetic model.

2.4. Analytical methods

The quantification of MNZ concentration was carried out with a Shimadzu high-performance liquid chromatography (HPLC, Prominence-I LC-2030 C), equipped with a reverse phase C18 column (Eclipse Plus 5 μm, Agilent) and a diode array detector (SPDM30 A). An isocratic method was established using a mobile phase composed of acetonitrile and 0.1% acetic acid aqueous solution (20:80, v/v) with a flow rate of 0.6 $mL{\cdot}min^{-1}$, setting the wavelength at 319 nm for an optimum MNZ detection. The byproducts of MNZ photodegradation were identified by electrospray ionization-mass spectrometry coupled to a liquid chromatograph (LC/ESI-MS). The mass detector operates in positive ion mode, setting the captive-spray source parameters as follows: a capillary voltage of +3500 V, an endplate offset voltage of 500 V, a dry gas flow rate of 8.0 $L{\cdot}min^{-1}$ at 300 °C, whereas the mass scan was conducted over the range 50−3000 *m/z*. A Shimazu TOC-L analyzer was used to quantify the total organic carbon (TOC). Quantification of short-chain carboxylic acids was performed by HPLC using a Supelcogel™ C610H column (9 μm, Aldrich). An isocratic method, with a 0.1% H_3PO_4 as mobile phase and a flow rate of 0.5 $mL{\cdot}min^{-1}$, was established. A Shimadzu 2501PC UV-Vis spectrophotometer was used to perform the turbidity tests. Photocatalyst suspensions were prepared under stirring at different photocatalyst dosages, from 50 to 750$mg{\cdot}L^{-1}$, and transferred to a 4 mL quartz cuvette to record the light absorbance at 600 nm. A blank with deionized water and without photocatalyst was used as a reference. The pH at the point of zero charge (pH_{pzc}) is defined as the value where the surface charge of a material is zero, determined by the pH drift method [35,36]. For this purpose, the pH of several NaCl solutions (0.01 M, 50 mL) was adjusted with the required amount of NaOH (0.1 M) or HCl (0.1 M) to a range from 2 to 11 (pH ≈ 2, 3, 4, 5, 7, 9, 11). This pH was recorded and named $pH_{initial}$. Then, 0.15 g of UiO-66-NH_2 was dispersed in those solutions, recording the pH after stirring for 24 h called pH_{final}. A curve is obtained by plotting the pH_{final} versus the $pH_{initial}$. The intersection point of this curve with the linear ratio between $pH_{final}/pH_{initial}$ provides the pH_{PZC} value. The morphology of MOF was evaluated by scanning electron microscopy (SEM) using Quanta 3D FEG (FEI company).

2.5. Theoretical calculation

All calculations of density functional theory (DFT) were performed using the Vienna Ab initio simulation package (VASP) to understand the

Table 1
ATA release after 24 h immersion in water at different pH values.

pH value	C_{ATA}-24 h	ATA leached-24 h
2.0	0.22 mg·L^{-1}	1.31%
3.2	n.d.	n.d.
4.3	n.d.	n.d.
5.2	n.d.	n.d.
7.3	n.d.	n.d.
9.22	n.d.	n.d.

n.d.: not detected

relationship between the molecular structure of MNZ and the degradation pathway [37]. The generalized gradient approximation (GGA) was adopted and the Perdew-Burke-Ernzerhof (PBE) functional was chosen to calculate the exchange-correlation potential with an energy cutoff of 500 eV [38,39]. After structure optimization, single point calculations were performed to obtain the molecular electrostatic potential at each of the nuclei. The electrostatic potential (ESP) and Fukui index involved in the analysis were evaluated based on an efficient algorithm proposed by the multifunctional wavefunction analyzer (Multiwfn) [40,41]. The distribution of HOMO and LUMO orbitals and the ESP were visualized using Visual Molecular Dynamics (VMD) software [42].

2.6. Ecotoxicity assessment

Ecological Structure-Activity Relationship Class Program (ECOSAR V2.0) software from the US Environmental Protection Agency was used to theoretically evaluate the acute toxicity of MNZ and its degradation byproducts [43,44], including both the acute and chronic toxicity for three different trophic levels organisms (i.e., fish, daphnids, and green algae). Furthermore, according to the Globally Harmonized System of Classification and Labelling of Chemicals (GHS) (United Nations, 2011) [43,45], the predicted toxicity values are classified into four levels, i.e., very toxic, toxic, harmful and not harmful. The predicted no-effect concentration is based on the toxicity data of the compound, such as the LC_{50} (96 h/48 h Half-maximal lethal concentration for fish and daphnia population, respectively), EC_{50} (96 h Half effective concentration for green algae growth) in acute toxicity and ChV (Chronic value).

3. Result and discussion

3.1. Properties of UiO-66-NH_2

UiO-66-NH_2 consists of $[Zr_6O_6(OH)_4]^{12+}$ secondary building units (SBUs) connected by 2-aminoterephthalate linkers to form a 12-connected structure with a face-centered cubic (fcc) topology [46,47]. We previously synthesized and characterized the UiO-66-NH_2 for the degradation of acetaminophen under simulated sunlight [33]. All characterization results are included in the supplementary information in Figs. S1-S6. Among them, are highlighted the positions of the conduction and valence bands that are located at − 0.68 and 2.13 V, respectively. Since the aim is to deepen the use of UiO-66-NH_2 for water treatment, its stability in water should be studied in more detail to learn about its structural consistency during the photocatalytic reaction. For this purpose, UiO-66-NH_2 was exposed to aqueous solutions at different pH (3.0 g·L^{-1}, 24 h) and the concentration of the leached linker was measured by HPLC, establishing the leachate percentage by the following equation [35,48]:

$$\text{Leachate}\ (\%) = \frac{C_{ATA}}{C_{UiO\text{-}66\text{-}NH_2}} \times \frac{M_{UiO\text{-}66\text{-}NH_2}}{24 \times M_{ATA}} \times 100$$

The nominal formula of UiO-66-NH_2 is $Zr_{24}O_{120}C_{192}H_{96}N_{24}$ [49], with a molecular weight of 6848.1 g·mol^{-1} ($M_{UiO\text{-}66\text{-}NH2}$), which contains 24 ATA molecules with a total molecular weight of 181.1 g·mol^{-1} (M_{ATA}). $C_{UiO\text{-}66\text{-}NH2}$ is the concentration of MOF used in each essay and

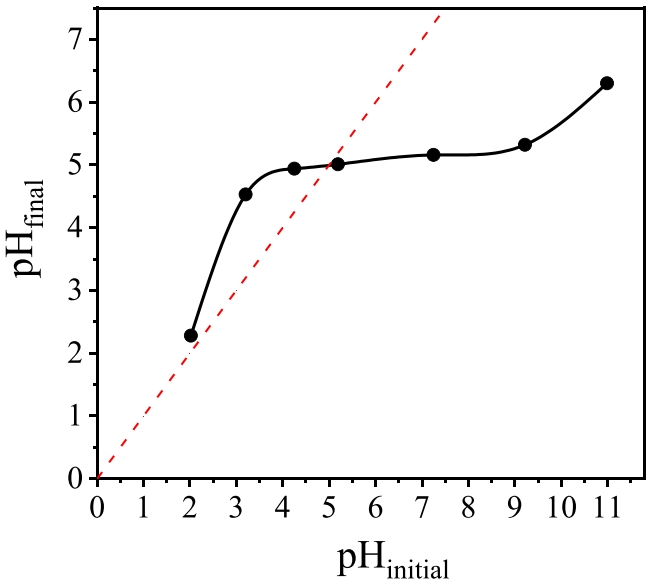

Fig. 1. Determination for pH_{pzc} of UiO-66-NH_2 by the drift method.

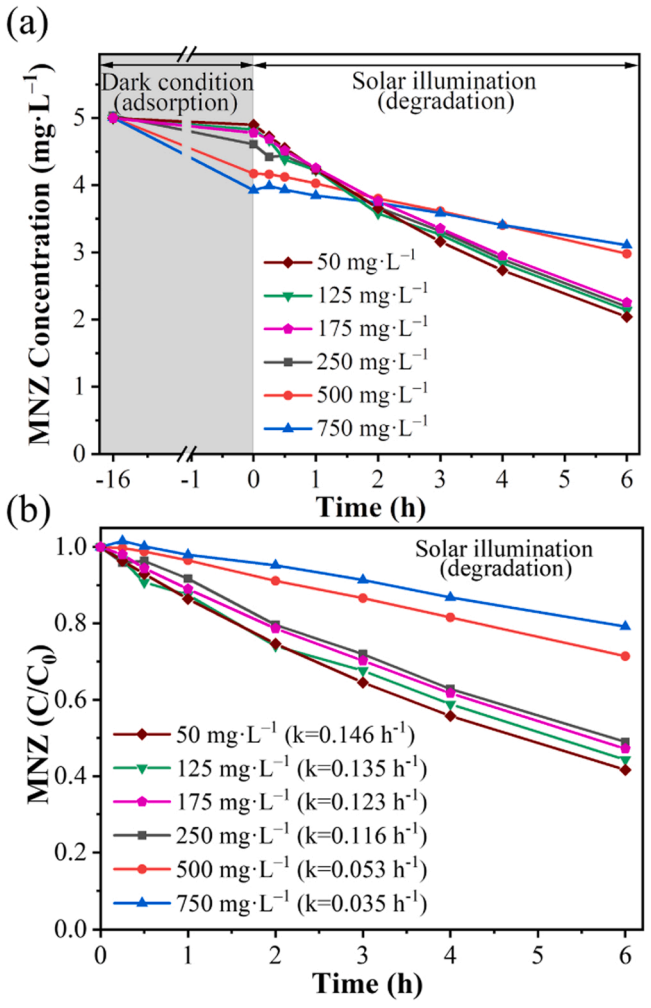

Fig. 2. (a) Effect of UiO-66-NH_2 dosage on adsorption and photocatalytic degradation of MNZ; and (b) evolution of MNZ with the irradiation time at different catalyst dosage (Intensity = 600 W·m^{-2}; $[MNZ]_0$ = 5 mg·L^{-1}).

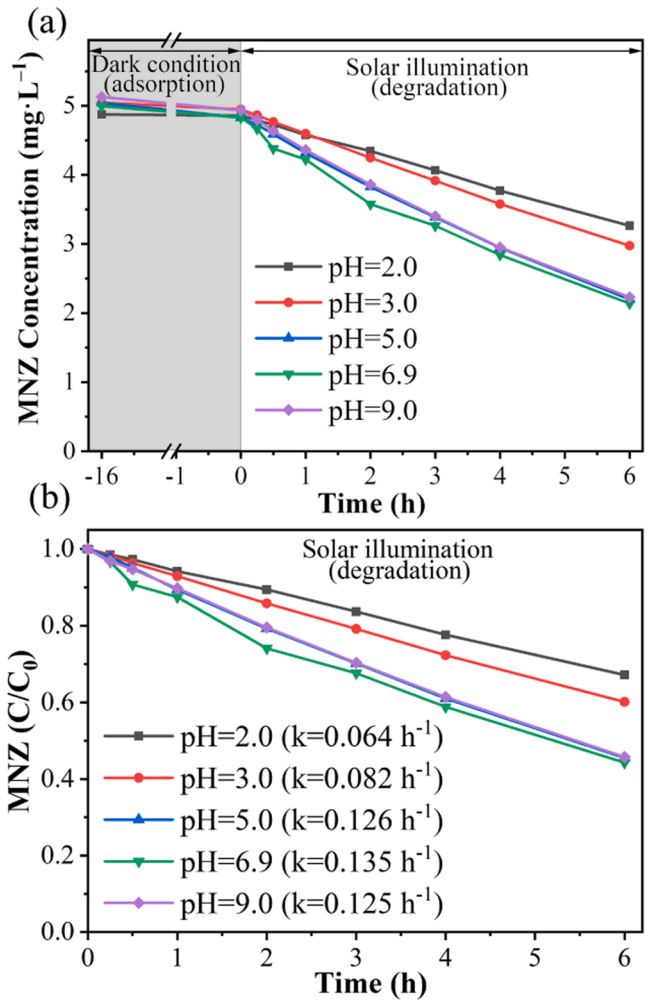

Fig. 3. (a) Effect of initial pH value on adsorption and photocatalytic degradation of MNZ; and (b) evolution of MNZ with the irradiation time at different pH values (Intensity = 600 W·m^{-2}; [MNZ]$_0$ = 5 mg·L^{-1}, [photocatalyst] = 125 mg·L^{-1}).

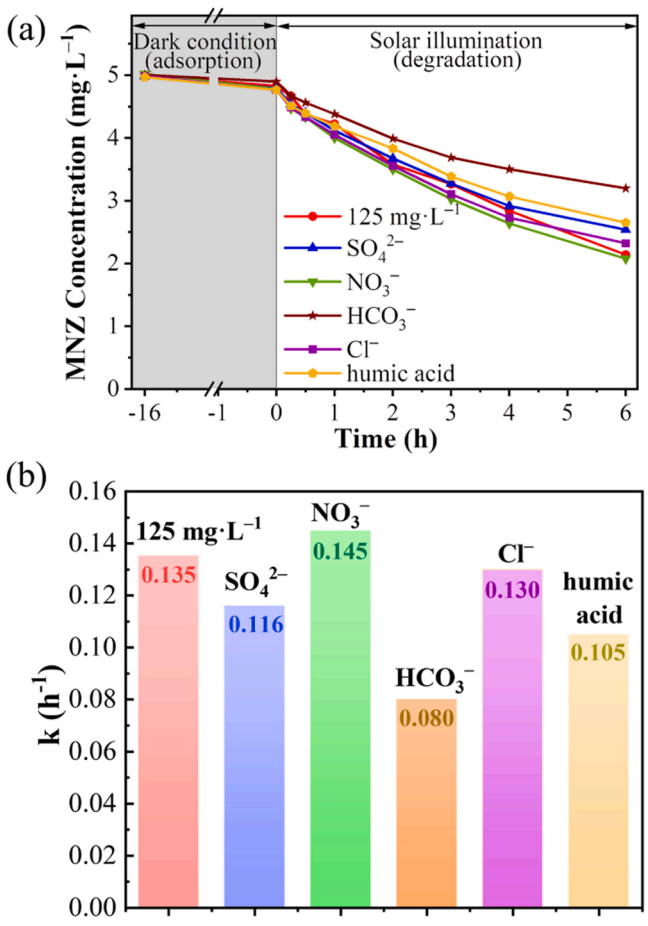

Fig. 4. (a) Evolution of MNZ concentration in the presence of NO_3^-, Cl^-, SO_4^{2-}, HCO_3^- and humic acid; and (b) pseudo-first-order rate constants (k, R^2 >0.99) (Intensity = 600 W·m^{-2}; [MNZ]$_0$ = 5 mg·L^{-1}, [photocatalyst] = 125 mg·L^{-1}).

C_{ATA} is the ATA concentration detected in the aqueous solution. Table 1 summarizes the ATA leached to the water solution after 24 h at different pH values. As can be seen, the MOF is quite stable with no linker leaching at most tested pHs. Only at the most acidic pH used (pH =2) a low ATA leaching was observed accounting for less than 1.5% of the total ATA content of the MOF. Thus, it can be concluded that the MOF is very stable in water, which is crucial for potential applications.

Once the stability of the UiO-66-NH_2 has been analyzed, another relevant parameter for the removal of pollutants in water is the pH at the point of zero charge (pH_{pzc}) to understand the affinity of the catalyst surface to the target pollutant. Fig. 1 depicts the determination of the pH_{pzc} of UiO-66-NH_2 by the drift method [50,51], resulting in a value of 5.0, analogous to that reported in the literature [35,52]. This value assumes that operating at pH < 5.0 the MOF surface is positively charged, while it is negatively charged at pH > 5.0. With a pKa1 value of 2.58 for imidazole nitrogen and 14.44 (pKa2) for the phenol group [53], MNZ exists almost in the protonated form at pH < 2.58 due to deprotonation of the carbonyl group, while at pH ≥ 2.58 it exists in the natural form [54,55]. The pKa value and pH_{pzc} may play a major role during the adsorption at different pH values. Adsorption is favoured when the target molecule charge is opposite to the catalyst surface charge, while electrostatic repulsion creates a barrier to hinder adsorption when both the target molecule and the catalyst surface have the same charge [56]. This issue will be revisited in Section 3.2 when the effect of pH on the adsorption and photodegradation of MNZ will be discussed.

3.2. Photocatalytic performance of MNZ photodegradation

The application in real aquatic environments is often influenced by many factors. Therefore, the effects of catalyst dosage, initial pH, and initial MNZ concentration on MNZ degradation were explored. Fig. 2**a** depicted the effect of catalyst dosage on MNZ adsorption and photodegradation. As expected, increasing the catalyst dosage (from 50 to 750 mg·L^{-1}) increases the percentage of MNZ retained by adsorption. The opposite behaviour is observed during the photocatalytic reaction (Fig. 2**b**). The MNZ photodegradation worsens as the catalyst dosage increases, with a considerable reduction in the reaction rate.

The use of high doses of the catalyst increases the solution turbidity, as was observed during the turbidity tests (Fig. S7). As the photocatalyst dosage increases, the light transmission into the suspension decreases which partially scatters direct light and reduces photoexcitation. In addition, self-depletion of free radicals can occur with a large catalyst dosage that impairs the photocatalytic reaction [7,57]. Based on these results, the catalyst dosage was set at 125 mg·L^{-1} in the subsequent experiments.

The effect of the solution pH on the photocatalytic performance of the UiO-66-NH_2 was further evaluated, showing the results in Fig. 3**a**. At the catalyst dose used the MNZ adsorption was almost negligible at all the pH values tested. This behaviour indicates that electrostatic forces are not significant in the adsorption process. If these forces were involved, the adsorption should be higher at low pH values (pH =2), since at this pH the surface of the MOF and the MNZ molecules should be

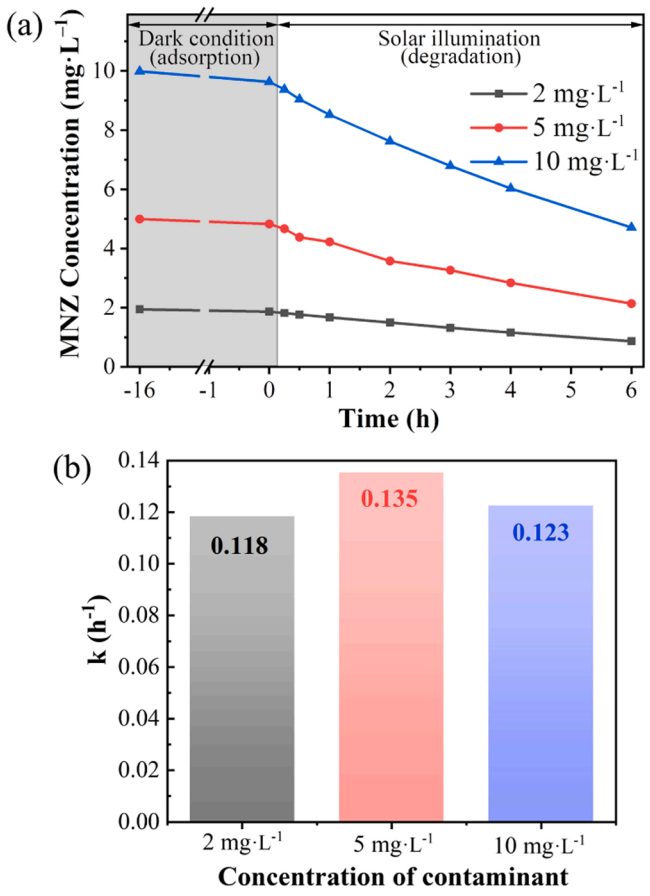

Fig. 5. (a) Effect of MNZ initial concentration on adsorption and photocatalytic degradation; and (b) pseudo-first-order rate constants (k, R^2 >0.99) (Intensity = 600 W·m^{-2}; [photocatalyst] = 125 mg·L^{-1}).

positively and negatively charged, respectively, resulting in an increase in the amount adsorbed by attractive electrostatic forces. In contrast, pH produces noticeable changes in the photocatalytic performance of the UiO-66-NH_2, as can be seen in Fig. 3**b**. MNZ conversion decreases when operating at pH below 5, registering the best kinetic rates at values close to the natural pH of MNZ (c.a. 6.9). This is most likely due to the scavenging effect of the protons in the aqueous solution, which can recombine with some of the radicals (e.g., hydroxyl radicals) thus reducing the photocatalytic activity [58]. Since the stability of the MOF can be an important drawback in this application, the structure and morphology of the UiO-66-NH_2 were characterized after contact with the solutions at the most extreme pH values, 2 and 9. The crystalline structure and morphology, determined respectively by XRD and SEM, remained unchanged, which confirmed the stability of the MOF at these pH values (Fig. S8, S9).

The presence of inorganic anions (such as Cl^-, NO_3^-, SO_4^{2-} or HCO_3^-) and humic acid has been reported to interfere with the role of the radical species, mainly $^{\bullet}OH$, during the degradation of organic pollutants [59]. Thus, individual MNZ degradation essays were explored in presence of the above inorganic anions and humic acid at environmentally relevant concentrations (Fig. 4). NO_3^-, Cl^- and SO_4^{2-} showed a negligible impact on the photocatalytic performance. These anions can compete with the target compound for the $^{\bullet}OH$ [59], but, since the $^{\bullet}OH$ contribution for MNZ degradation is minor compared with other radicals, its presence does not affect the performance. HCO_3^- showed a slightly negative impact on MNZ degradation, since it can compete with the photogenerated h^+, $^{\bullet}OH$, and $^{\bullet}O_2^-$ radicals [60,61]. The inhibitory effect of humic acid was also negligible, maintaining the photocatalytic performance of the UiO-66-NH_2.

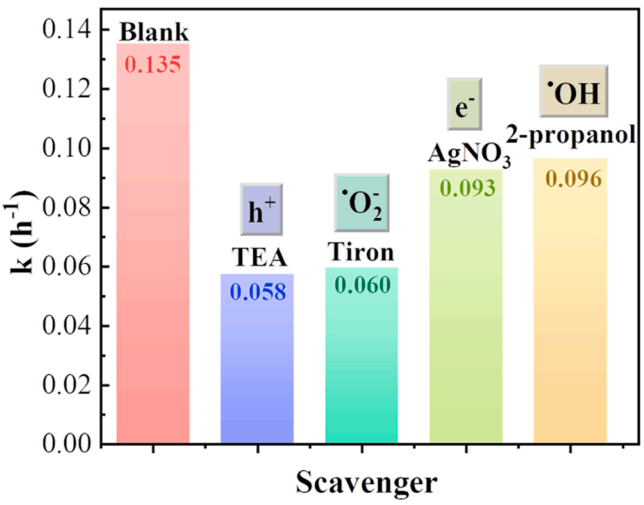

Fig. 6. Pseudo-first-order rate constants (k) of MNZ disappearance by photocatalytic degradation with UiO-66-NH_2 in the presence of different scavengers (Intensity = 600 W·m^{-2}; $[MNZ]_0$ = 5 mg·L^{-1}; [photocatalyst] = 125 mg·L^{-1}; [scavenger] = 1 mM).

Fig. 5**a** represents the evolution of the photocatalytic performance of the UiO-66-NH_2 upon irradiation time with different initial concentrations of MNZ. The adsorption capacity of the UiO-66-NH_2 slightly increases with the initial MNZ concentration, although it can be considered negligible at all the MNZ concentrations tested. Regarding the photodegradation process, the reaction rate remained very similar (Fig. 5**b**), indicating that the UiO-66-NH_2 is able to promote the generation of an adequate number of active species and radicals. To learn about the species responsible for MNZ degradation, further essays were conducted with different scavengers, using TEA, Tiron, $AgNO_3$ and 2-propanol as scavengers of holes (h^+), superoxide radicals ($^{\bullet}O_2^-$), photogenerated electrons (e^-) and hydroxyl radicals ($^{\bullet}OH$), respectively [35, 62,63]. Fig. 6 shows the changes suffered on the pseudo-first-order rate

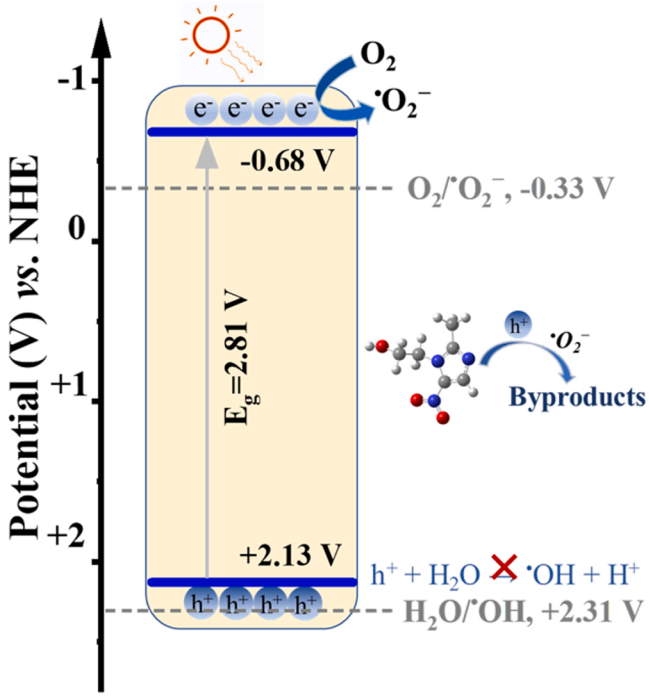

Fig. 7. Proposed photocatalytic charge transfer mechanism over UiO-66-NH_2 for the MNZ degradation.

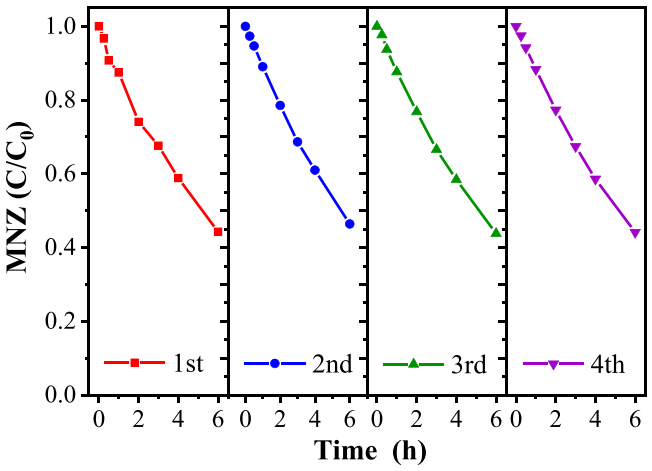

Fig. 8. Evolution of MNZ versus reaction time in four-cycle tests with UiO-66-NH_2 (Intensity = 600 W·m^{-2}; $[MNZ]_0$ = 5 mg·L^{-1}; [photocatalyst] = 125 mg·L^{-1}).

constant (k) of MNZ disappearance by photodegradation in the absence and presence of the different scavengers. The addition of both TEA and Tiron considerably limits the MNZ degradation, so both h^+ and $^{\bullet}O_2^-$ play a key role in the photocatalytic reaction. Meanwhile, the addition of both 2-propanol and $AgNO_3$ reduces the activity but causes much less effect, indicating that the contribution of $^{\bullet}OH$ radicals and the photo-generated electrons must be of lower significance.

We have compared the performance of our photocatalyst with those of other recently reported. In this sense, In this sense, Sheikhsamany et al. [64] obtained a degradation efficiency of 43% in 4 h for the photodegradation of MNZ using SnO_2/MOF-199 under visible light. Balasurya et al. [65] reported a photodegradation rate constant of 0.150 h^{-1} using a $CaMoO_4$-Ag_2MoO_4 nanohybrid under visible light exposure (500 W tungsten lamp). Aoudjit et al. [66] obtained a value higher than 0.531 h^{-1} when analyzing the MNZ oxidation with hybrids of semiconductors (MoO_3, CuO) and layered double hydroxides under solar irradiation. It should be underlined that in this case, the study used a high photocatalyst load (1500 mg·L^{-1}). Finally, Fu et al. [67] achieved a MNZ photodegradation rate constant of 0.522 h^{-1} using a 500 W Xenon lamp and a Z-scheme MoS_2/Ag_2CO_3 photocatalyst. It should be mentioned that higher first order rate constants for the photo-degradation of MNZ can be founded in the literature. However, it is noteworthy that the comparison is not easy, since most of them use other types of irradiation or add some oxidizing agents or use very different

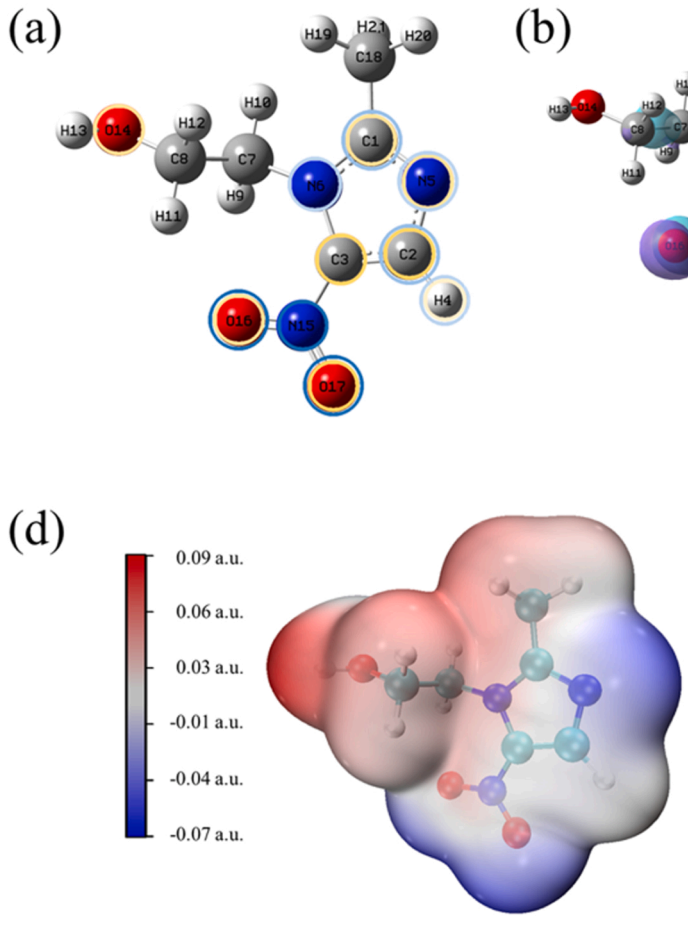

(e)

Atom	q(N)	q(N+1)	q(N-1)	f^-	f^+
1(C)	0.1043	0.0293	0.1982	0.0939	0.075
2(C)	0.0014	-0.0928	0.103	0.1016	0.0942
3(C)	0.0338	0.0103	0.1547	0.1209	0.0235
4(H)	0.0666	0.0245	0.1115	0.0449	0.0421
5(N)	-0.1973	-0.2564	-0.1195	0.0778	0.0591
6(N)	0.0009	-0.0303	0.0339	0.0329	0.0312
7(C)	0.0083	-0.0008	0.0192	0.0109	0.0091
8(C)	0.0226	0.0152	0.0391	0.0165	0.0074
9(H)	0.0471	0.0362	0.0642	0.0171	0.0109
10(H)	0.0464	0.0255	0.066	0.0196	0.0209
11(H)	0.0287	0.0277	0.0453	0.0167	0.0009
12(H)	0.0239	0.0109	0.0419	0.018	0.013
13(H)	0.1741	0.156	0.2029	0.0288	0.0181
14(O)	-0.235	-0.2532	-0.1701	0.0649	0.0182
15(N)	0.2352	0.118	0.2563	0.021	0.1173
16(O)	-0.2155	-0.3886	-0.1392	0.0763	0.1731
17(O)	-0.2185	-0.3964	-0.1086	0.1099	0.1779
18(C)	-0.0758	-0.1003	-0.0463	0.0295	0.0245
19(H)	0.0451	0.0163	0.0792	0.0341	0.0287
20(H)	0.0561	0.0316	0.0837	0.0277	0.0244
21(H)	0.0476	0.0173	0.0846	0.037	0.0303

Fig. 9. (a) The chemical structure, (b) HOMO and (c) LUMO orbitals distribution, (d) ESP mapping, and (e) Fukui index of MNZ molecule.

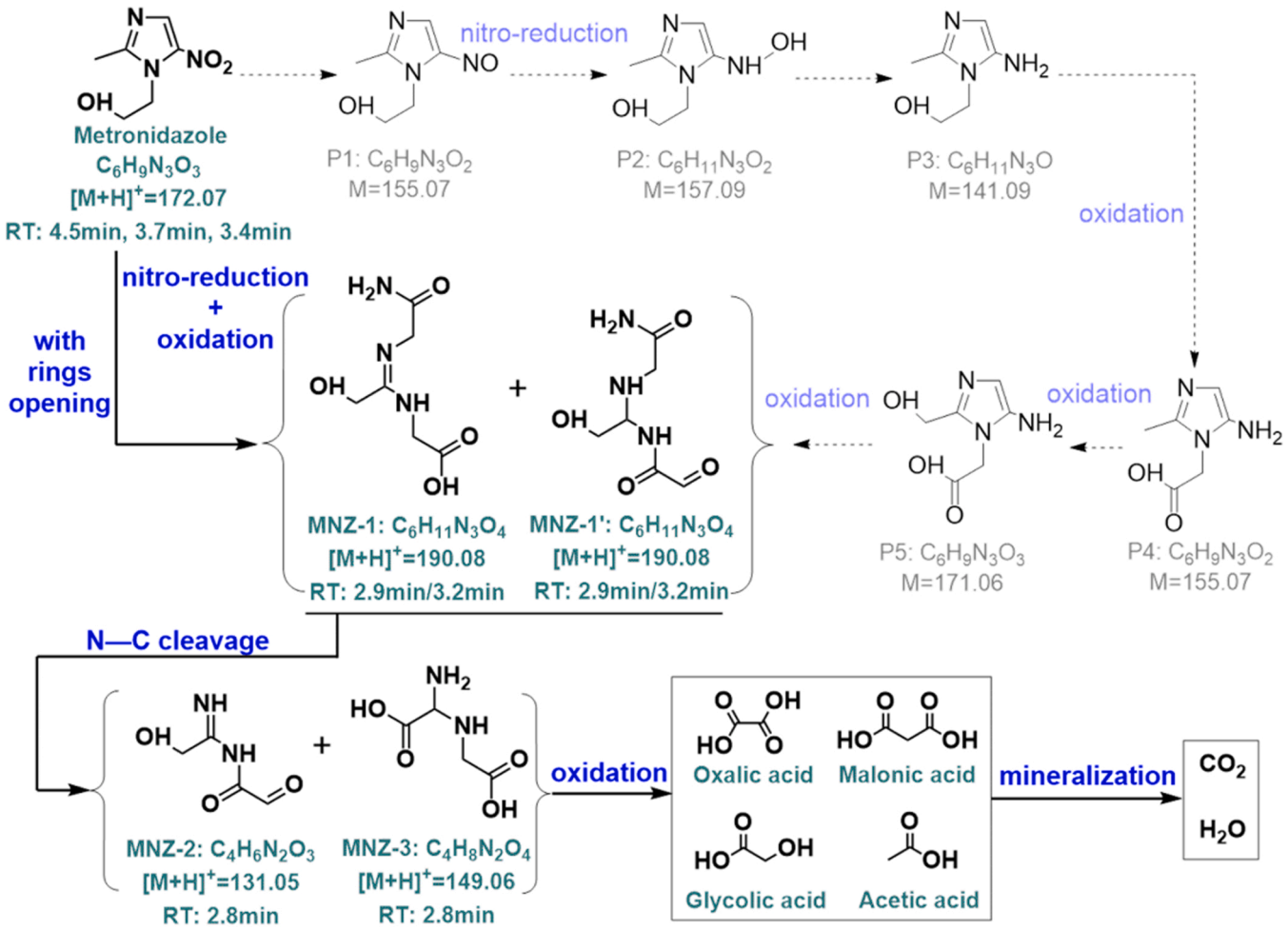

Fig. 10. Proposed photodegradation pathway of MNZ with UiO-66-NH_2 (the grey part with dashed arrows shows undetected byproducts).

reaction conditions [68–71].

Based on the results of quenching tests, Fig. 7 presents a plausible mechanism for the photodegradation of MNZ using UiO-66-NH_2, considering the band alignments established previously [33]. Under light irradiation, the UiO-66-NH_2 absorbs the light yielding the migration of electrons from the valence band (VB) to the conduction band (CB), thus appearing h^+ in the VB and photogenerated e^- in the CB. Since the standard redox potential of superoxide radicals ($E(O_2/^{\bullet}O_2^-)$ = −0.33 V vs NHE) [72] is less negative than the CB of UiO-66-NH_2, the photogenerated e^- can interact with the O_2 of the medium yielding to $^{\bullet}O_2^-$ radicals, as the reaction stated in Fig. 7. Conversely, since the VB of UiO-66-NH_2 is above the redox potential of $^{\bullet}OH$ ($E(H_2O/^{\bullet}OH)$ = 2.31 V vs NHE) [73], it is unlikely that h^+ reacts with water to generate $^{\bullet}OH$ radicals. Since the $^{\bullet}OH$ radicals play some role in the reaction, their formation should be due to the consequent reactions involving the $^{\bullet}O_2^-$ radicals through the formation of H_2O_2 [74–76]. The direct reaction of the $^{\bullet}O_2^-$ and h^+ is noteworthy in the mechanism described by the UiO-66-NH_2, which together with $^{\bullet}OH$ radicals and the photogenerated e^- attack the MNZ molecule, leading to chemical bonding breakage and its degradation.

The stability and recyclability of the photocatalyst are important issues regarding its potential application. Recycling tests were carried out to check the stability and recyclability of UiO-66-NH_2 (Fig. 8). After repeated collection by filtering and drying of the previous photocatalyst, the performance of the original UiO-66-NH_2 was well maintained. After four successive reuses, the UiO-66-NH_2 showed almost unaltered photocatalytic performance with a MNZ conversion close to 56% under the testing conditions.

3.3. DFT calculations and degradation pathways

Fig. 9**a-c** show the chemical structure of the MNZ molecule and its highest occupied molecular orbital (HOMO) and lowest unoccupied molecular orbital (LUMO), determined by DFT calculations. The purple and blue regions represent, respectively, the electron-rich and electron-poor regions of the MNZ molecule. HOMO and LUMO are generally used to describe the locations where organic target molecules tend to lose or gain electrons during a redox reaction [77,78]. As shown in Fig. 9**b-c**, electron clouds of the HOMO and the LUMO are mainly scattered into nitrogenous heterocycle and nitro group; hence h^+, $^{\bullet}OH$, $^{\bullet}O_2^-$ and photogenerated electrons are more likely to attack these vulnerable sites [79–81]. Fig. 9**d** shows the electrostatic potential (ESP) of the MNZ molecule; the red region has a positive electrostatic potential, indicating that this region is more accessible to electrons and more electrophilic compared to other regions [78]. From the perspective of electrostatic potential, the hydroxyl group of the MNZ located near the highest value of ESP (0.09 a.u.), with a positive potential, is more likely to attract the negatively charged $^{\bullet}O_2^-$ species. Fig. 9**e** lists the Fukui index for the different sites of MNZ, which can be inferred as information about the type and ease of attack of the atoms during MNZ degradation. Higher values of f^- and f^+ indicate that the corresponding sites are more prone to nucleophilic and electrophilic radicals attack, respectively. Overall, both the sites located on the MNZ heterocycle ring and the non–C–C and non–C–H bonds outside the heterocycle are vulnerable to attack by free radicals.

The degradation byproducts of MNZ were identified by LC/ESI-MS and their mass spectra are shown in Fig. S10. Only four byproducts

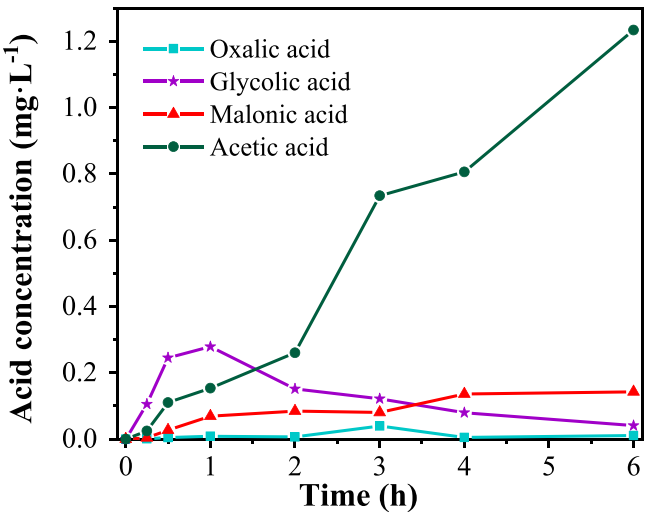

Fig. 11. Evolution of short-chain carboxylic acids detected during MNZ photodegradation with UiO-66-NH_2 (Intensity = 750 W·m^{-2}; $[MNZ]_0$ = 5 mg·L^{-1}; [photocatalyst] = 125 mg·L^{-1}).

were detected by this technique, shown in Table S1, whose formation can follow the degradation pathway proposed in Fig. 10. MNZ molecules undergo the ring-opening together with nitro-reduction and oxidation reactions leading to the generation of the detected MNZ1 byproduct, appearing as two isomers (MNZ1 and MNZ1′) at the same retention time in the chromatogram. The literature describes how MNZ suffers the successive nitro-reduction and oxidation reactions, yielding to the intermediates P1-P5 shown in Fig. 10 but not detected in our essays. P1 was generated by the reduction of the nitro group, which undergoes further nitro-reductions yielding to P2 and subsequent P3 intermediates. P3 can be further oxidized generating P4 which continues to oxidize, resulting in the formation of P5 intermediate [82–84]. Its further oxidation and heterocycle ring opening result in the generation of MNZ-1 and MNZ-1′ isomers. Subsequently, the N–C cleavage occurs and the byproducts MNZ-2 and MNZ-3 appear. This pathway agrees with theoretical calculations and the Fukui index, as both the heterocycle ring and the nitro group were established as the more vulnerable to radical attack. As a novelty, it is noteworthy that the byproducts herein detected have not been previously reported in the photodegradation of MNZ with other photocatalysts. The further evolution of these byproducts, MNZ-2 and MNZ-3, to smaller molecules was analyzed by changing the HPLC detection method. Four short-chain carboxylic acids were identified, oxalic, malonic, glycolic and acetic acids, which evolution with the reaction time is depicted in Fig. 11. Glycolic acid concentration tends to increase at the start of the reaction, further decreasing over longer reaction times. The opposite effect occurs with acetic acid, since its concentration increases along the reaction, being the main short-chain carboxylic acid detected at the end of the reaction. A higher intensity light source was carried out to degrade the MNZ to achieve higher conversion efficiency, in Fig. S11 the light intensity was increased from 600 to 750 W·m^{-2} and the degradation efficiency increased from 56% to 68%. Although different byproducts were detected after 6 h of reaction, the mineralization achieved for MNZ and byproducts was quite high, quantifying a TOC conversion of 56%, quite high considering the MNZ conversion (68%).

3.4. Toxicity assessment

The predicted acute and chronic toxicity of the detected photodegradation byproducts were theoretically determined using ECOSAR software [44,85,86]. The half-lethal concentration, half-effective concentration and chronic toxicity are important indicators to assess the toxicity to aquatic animals due to the presence of water pollutants. The LC_{50}, EC_{50}, and ChV values of all byproducts, including short-chain carboxylic acids, were higher than those of MNZ (Fig. 12), confirming that all of them have lower toxicity than the initial MNZ. Regarding acute toxicity, all byproducts were non-toxic, while regarding chronic toxicity, only MNZ-2 was classified as harmful in relation to the Daphnia model. Based on these results, it can be concluded that UiO-66-NH_2 is suitable for the removal of MNZ by photocatalytic breakdown under solar radiation.

4. Conclusions

In this work, the performance and mechanism of metronidazole

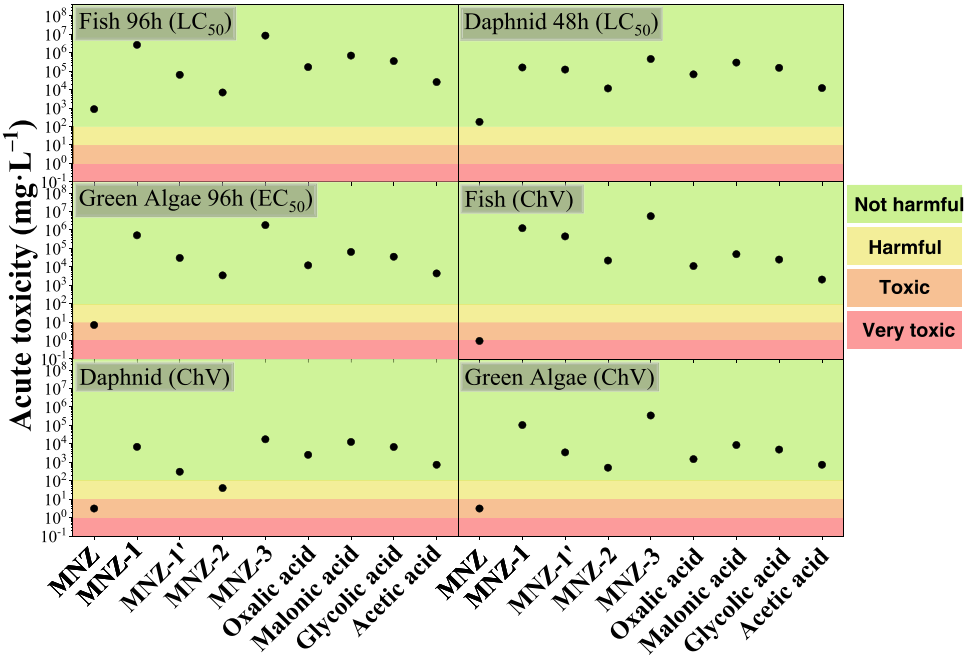

Fig. 12. LC_{50}, EC_{50}, and ChV values of MNZ and the detected byproducts on fish, daphnia and green algae.

removal by UiO-66-NH_2 were investigated under simulated sunlight. UiO-66-NH_2 maintained good MNZ removal efficiency under the conditions of a 5.0–9.0 pH range in an aqueous solution, low catalyst dosage, and a wide range of pollutant concentrations. During the photodegradation of MNZ, h^+, $^{\bullet}O_2^-$, $^{\bullet}OH$ and photogenerated electrons act as active species simultaneously, with h^+ and $^{\bullet}O_2^-$ playing a dominant role. In addition, UiO-66-NH_2 showed excellent stability and reusability in the recycling experiments. DFT calculations explain that the active species more readily attack the nitrogen-containing heterocycle and nitro group in metronidazole. In the degradation pathway, metronidazole undergoes a series of oxidation, nitro-reduction and ring-opening processes and four non-previously described byproducts were detected for the first time. Correspondingly, toxicological simulations showed that the toxicity of all byproducts of MNZ was reduced upon photodegradation. This work provides a deeper insight into the mechanism of photodegradation of metronidazole by UiO-66-NH_2.

Declaration of Competing Interest

The authors declare that they have no known competing financial interests or personal relationships that could have appeared to influence the work reported in this paper.

Data Availability

Data will be made available on request.

Acknowledgements

This work was supported by the National State Research Agency of Spain (project number: PID2019–106186RB-I00/AEI/10.13039/501100011033). Yilan Wang acknowledges the financial support provided by China Scholarship Council (CSC No. 201908610198). The authors sincerely acknowledged support from the external services of the Autonomous University of Madrid (SIdI).

Authorship contribution statement

The manuscript was written with the contributions of all authors. All authors have given approval for the final version of the manuscript.

Appendix A. Supporting information

Supplementary data associated with this article can be found in the online version at doi:10.1016/j.jece.2023.109744.

References

[1] M. Tian, X. He, Y. Feng, W. Wang, H. Chen, M. Gong, D. Liu, J.L. Clarke, A. Van Eerde, Pollution by antibiotics and antimicrobial resistance in livestock and poultry manure in china, and countermeasures, Antibiot. 10 (2021) 539, https://doi.org/10.3390/ANTIBIOTICS10050539.

[2] A. Christou, A. Agüera, J.M. Bayona, E. Cytryn, V. Fotopoulos, D. Lambropoulou, C. M. Manaia, C. Michael, M. Revitt, P. Schröder, D. Fatta-Kassinos, The potential implications of reclaimed wastewater reuse for irrigation on the agricultural environment: the knowns and unknowns of the fate of antibiotics and antibiotic resistant bacteria and resistance genes – a review, Water Res. 123 (2017) 448–467, https://doi.org/10.1016/J.WATRES.2017.07.004.

[3] K.G. Karthikeyan, M.T. Meyer, Occurrence of antibiotics in wastewater treatment facilities in Wisconsin, USA, Sci. Total Environ. 361 (2006) 196–207, https://doi.org/10.1016/J.SCITOTENV.2005.06.030.

[4] O. Baaloudj, I. Assadi, N. Nasrallah, A. El Jery, L. Khezami, A.A. Assadi, Simultaneous removal of antibiotics and inactivation of antibiotic-resistant bacteria by photocatalysis: a review, J. Water Process Eng. 42 (2021), 102089, https://doi.org/10.1016/J.JWPE.2021.102089.

[5] A.S. Ezeuko, M.O. Ojemaye, O.O. Okoh, A.I. Okoh, Potentials of metallic nanoparticles for the removal of antibiotic resistant bacteria and antibiotic resistance genes from wastewater: a critical review, J. Water Process Eng. 41 (2021), 102041, https://doi.org/10.1016/J.JWPE.2021.102041.

[6] F.S. Mustafa, A.A. Oladipo, Photocatalytic degradation of metronidazole and bacteria disinfection activity of Ag–doped $Ni_{0.5}Zn_{0.5}Fe_2O_4$, J. Water Process Eng. 42 (2021), 102132, https://doi.org/10.1016/J.JWPE.2021.102132.

[7] F. Bashiri, S.M. Khezri, R.R. Kalantary, B. Kakavandi, Enhanced photocatalytic degradation of metronidazole by TiO_2 decorated on magnetic reduced graphene oxide: characterization, optimization and reaction mechanism studies, J. Mol. Liq. 314 (2020), 113608, https://doi.org/10.1016/J.MOLLIQ.2020.113608.

[8] M. Ahmad, I. Ahmad, E. Ahmed, M.S. Akhtar, N.R. Khalid, Facile and inexpensive synthesis of Ag doped ZnO/CNTs composite: study on the efficient photocatalytic activity and photocatalytic mechanism, J. Mol. Liq. 311 (2020), 113326, https://doi.org/10.1016/J.MOLLIQ.2020.113326.

[9] R. Fahrig, M. Engelke, Reinvestigation of in vivo genotoxicity studies in man. I. No induction of DNA strand breaks in peripheral lymphocytes after metronidazole therapy, Mutat. Res. Toxicol. Environ. Mutagen. 395 (1997) 215–221, https://doi.org/10.1016/S1383-5718(97)00177-0.

[10] IARC Monographs on the Evaluation of Carcinogenic Risks to Humans, 2014.

[11] J.L. Wilkinson, A.B.A. Boxall, D.W. Kolpin, K.M.Y. Leung, R.W.S. Lai, C. Galban-Malag, A.D. Adell, J. Mondon, M. Metian, R.A. Marchant, A. Bouzas-Monroy, A. Cuni-Sanchez, A. Coors, P. Carriquiriborde, M. Rojo, C. Gordon, M. Cara, M. Moermond, T. Luarte, V. Petrosyan, Y. Perikhanyan, C.S. Mahon, C.J. McGurk, T. Hofmann, T. Kormoker, V. Iniguez, J. Guzman-Otazo, J.L. Tavares, F.G. de Figueiredo, M.T.P. Razzolini, V. Dougnon, G. Gbaguidi, O. Traore, J.M. Blais, L. E. Kimpe, M. Wong, D. Wong, R. Ntchantcho, J. Pizarro, G.G. Ying, C.E. Chen, M. Paez, J. Martınez-Lara, J.P. Otamonga, J. Pote, S.A. Ifo, P. Wilson, S. Echeverria-Saenz, N. Udikovic-Kolic, M. Milakovic, D. Fatta-Kassinos, L. Ioannou-Ttofa, V. Belusova, J. Vymazal, M. Cardenas-Bustamante, B.A. Kassa, J. Garric, A. Chaumot, P. Gibba, I. Kunchulia, S. Seidensticker, G. Lyberatos, H. P. Halldorsson, M. Melling, T. Shashidhar, M. Lamba, A. Nastiti, A. Supriatin, N. Pourang, A. Abedini, O. Abdullah, S.S. Gharbia, F. Pilla, B. Chefetz, T. Topaz, K. M. Yao, B. Aubakirova, R. Beisenova, L. Olaka, J.K. Mulu, P. Chatanga, V. Ntuli, N. T. Blama, S. Sherif, A.Z. Aris, L.J. Looi, M. Niang, S.T. Traore, R. Oldenkamp, O. Ogunbanwo, M. Ashfaq, M. Iqbal, Z. Abdeen, A. O'Dea, J.M. Morales-Saldaña, M. Custodio, H. de la Cruz, I. Navarrete, F. Carvalho, A.B. Gogra, B.M. Koroma, V. Cerkvenik-Flajs, M. Gombac, M. Thwala, K. Choi, H. Kang, J.L. Celestino Ladu, A. Rico, P. Amerasinghe, A. Sobek, G. Horlitz, A.K. Zenker, A.C. King, J.J. Jiang, R. Kariuki, M. Tumbo, U. Tezel, T.T. Onay, J.B. Lejju, Y. Vystavna, Y. Vergeles, H. Heinzen, A. Perez-Parada, D.B. Sims, M. Figy, D. Good, C. Teta, Pharmaceutical pollution of the world's rivers, Proc. Natl. Acad. Sci. U. S. A. 119 (2022), e2113947119, https://doi.org/10.1073/PNAS.2113947119/SUPPL_FILE/PNAS.2113947119.SD12.XLSX.

[12] M. Usman, Y.S. Ho, A bibliometric study of the Fenton oxidation for soil and water remediation, J. Environ. Manag. 270 (2020), 110886, https://doi.org/10.1016/J.JENVMAN.2020.110886.

[13] F. Daoud, D. Pelzer, S. Zuehlke, M. Spiteller, O. Kayser, Ozone pretreatment of process waste water generated in course of fluoroquinolone production, Chemosphere 185 (2017) 953–963, https://doi.org/10.1016/J.CHEMOSPHERE.2017.07.040.

[14] W.L. Wang, Q.Y. Wu, N. Huang, Z. Bin Xu, M.Y. Lee, H.Y. Hu, Potential risks from UV/H_2O_2 oxidation and UV photocatalysis: A review of toxic, assimilable, and sensory-unpleasant transformation products, Water Res. 141 (2018) 109–125, https://doi.org/10.1016/J.WATRES.2018.05.005.

[15] L. Yang, L. He, J. Xue, Y. Ma, Z. Xie, L. Wu, M. Huang, Z. Zhang, Persulfate-based degradation of perfluorooctanoic acid (PFOA) and perfluorooctane sulfonate (PFOS) in aqueous solution: review on influences, mechanisms and prospective, J. Hazard. Mater. 393 (2020), 122405, https://doi.org/10.1016/J.JHAZMAT.2020.122405.

[16] D. Chen, Y. Cheng, N. Zhou, P. Chen, Y. Wang, K. Li, S. Huo, P. Cheng, P. Peng, R. Zhang, L. Wang, H. Liu, Y. Liu, R. Ruan, Photocatalytic degradation of organic pollutants using TiO_2-based photocatalysts: A review, J. Clean. Prod. 268 (2020), 121725, https://doi.org/10.1016/J.JCLEPRO.2020.121725.

[17] X. Wang, L. Yin, G. Liu, Light irradiation-assisted synthesis of ZnO-CdS/reduced graphene oxide heterostructured sheets for efficient photocatalytic H_2 evolution, Chem. Commun. 50 (2014) 3460–3463, https://doi.org/10.1039/C4CC00044G.

[18] X. Wang, Q. Li, L. Gan, X. Ji, F. Chen, X. Peng, R. Zhang, 3D macropore carbon-vacancy g-C_3N_4 constructed using polymethylmethacrylate spheres for enhanced photocatalytic H_2 evolution and CO_2 reduction, J. Energy Chem. 53 (2021) 139–146, https://doi.org/10.1016/J.JECHEM.2020.05.001.

[19] M. Alsaidi, F.A. Azeez, L.A. Al-Hajji, A.A. Ismail, Impact of reaction parameters for photodegradation pharmaceuticals in wastewater over gold/titania photocatalyst synthesized by pyrolysis of NH_2-MIL-125(Ti), J. Environ. Manag. 314 (2022), 115047, https://doi.org/10.1016/J.JENVMAN.2022.115047.

[20] J. Cirkovic, A. Radojkovic, D. Lukovic Golic, N. Tasic, M. Cizmic, G. Brankovic, Z. Brankovic, Visible-light photocatalytic degradation of Mordant Blue 9 by single-phase $BiFeO_3$ nanoparticles, J. Environ. Chem. Eng. 9 (2021), 104587, https://doi.org/10.1016/J.JECE.2020.104587.

[21] H. Cai, D. Zhang, X. Ma, Z. Ma, A novel ZnO/biochar composite catalysts for visible light degradation of metronidazole, Sep. Purif. Technol. 288 (2022), 120633, https://doi.org/10.1016/J.SEPPUR.2022.120633.

[22] Hongli Liu, Xiaoyi Chang, Xiaoxun Liu, Li Guiying, Weiping Zhang, Taicheng An, Boosting the photocatalytic degradation of ethyl acetate by a Z-scheme Au–TiO_2@NH_2-UiO-66 heterojunction with ultrafine Au as an electron mediator, Environ. Sci. Nano. 8 (2021) 2542–2553, https://doi.org/10.1039/D1EN00225B.

[23] M.L. Tran, C.C. Fu, R.S. Juang, Removal of metronidazole by TiO_2 and ZnO photocatalysis: a comprehensive comparison of process optimization and transformation products, Environ. Sci. Pollut. Res. 25 (2018) 28285–28295, https://doi.org/10.1007/S11356-018-2848-7/FIGURES/8.

[24] M.L. Hsieh, R.S. Juang, Y.A. Gandomi, C.C. Fu, C. Te Hsieh, W.R. Liu, Synthesis and characterization of high-performance ZnO/graphene quantum dot composites for photocatalytic degradation of metronidazole, J. Taiwan Inst. Chem. Eng. 131 (2022), 104180, https://doi.org/10.1016/J.JTICE.2021.104180.

[25] Y. Qian, F. Zhang, H. Pang, Y. Qian, H. Pang, F. Zhang, A review of MOFs and their composites-based photocatalysts: synthesis and applications, Adv. Funct. Mater. 31 (2021) 2104231, https://doi.org/10.1002/ADFM.202104231.

[26] X. Zhao, J. Li, X. Li, P. Huo, W. Shi, Design of metal-organic frameworks (MOFs)-based photocatalyst for solar fuel production and photo-degradation of pollutants, Chin. J. Catal. 42 (2021) 872–903, https://doi.org/10.1016/S1872-2067(20)63715-9.

[27] X. Wang, Z. Cao, B. Du, Y. Zhang, R. Zhang, Visible-light-driven zeolite imidazolate frameworks-8@ZnO composite for heavy metal treatment, Compos. Part B Eng. 183 (2020), 107685, https://doi.org/10.1016/J.COMPOSITESB.2019.107685.

[28] R. Zhang, B. Du, Q. Li, Z. Cao, G. Feng, X. Wang, α-Fe_2O_3 nanoclusters confined into UiO-66 for efficient visible-light photodegradation performance, Appl. Surf. Sci. 466 (2019) 956–963, https://doi.org/10.1016/J.APSUSC.2018.10.048.

[29] X. Wang, X. Zhao, D. Zhang, G. Li, H. Li, Microwave irradiation induced UIO-66-NH_2 anchored on graphene with high activity for photocatalytic reduction of CO_2, Appl. Catal. B Environ. 228 (2018) 47–53, https://doi.org/10.1016/J.APCATB.2018.01.066.

[30] L. Shen, S. Liang, W. Wu, R. Liang, L. Wu, CdS-decorated UiO–66(NH_2) nanocomposites fabricated by a facile photodeposition process: an efficient and stable visible-light-driven photocatalyst for selective oxidation of alcohols, J. Mater. Chem. A. 1 (2013) 11473–11482, https://doi.org/10.1039/C3TA12645E.

[31] C. Zhao, Y. Li, H. Chu, X. Pan, L. Ling, P. Wang, H. Fu, C.C. Wang, Z. Wang, Construction of direct Z-scheme Bi_5O_7I/UiO-66-NH_2 heterojunction photocatalysts for enhanced degradation of ciprofloxacin: mechanism insight, pathway analysis and toxicity evaluation, J. Hazard. Mater. 419 (2021), 126466, https://doi.org/10.1016/J.JHAZMAT.2021.126466.

[32] Y.L. Wang, M. Peñas-Garzón, J.J. Rodriguez, J. Bedia, C. Belver, Enhanced photodegradation of acetaminophen over Sr@TiO_2/UiO-66-NH_2 heterostructures under solar light irradiation, Chem. Eng. J. 446 (2022), https://doi.org/10.1016/j.cej.2022.137229.

[33] Y.L. Wang, S. Zhang, Y.F. Zhao, J. Bedia, J.J. Rodriguez, C. Belver, UiO-66-based metal organic frameworks for the photodegradation of acetaminophen under simulated solar irradiation, J. Environ. Chem. Eng. 9 (2021), 106087, https://doi.org/10.1016/j.jece.2021.106087.

[34] V. Muelas-Ramos, C. Belver, J.J. Rodriguez, J. Bedia, Synthesis of noble metal-decorated NH_2-MIL-125 titanium MOF for the photocatalytic degradation of acetaminophen under solar irradiation, Sep. Purif. Technol. 272 (2021), 118896, https://doi.org/10.1016/J.SEPPUR.2021.118896.

[35] R.R. Solís, M. Peñas-Garzón, C. Belver, J.J. Rodriguez, J. Bedia, Highly stable UiO-66-NH_2 by the microwave-assisted synthesis for solar photocatalytic water treatment, J. Environ. Chem. Eng. 10 (2022), 107122, https://doi.org/10.1016/J.JECE.2021.107122.

[36] M. Peñas-Garzón, A. Gómez-Avilés, C. Belver, J.J. Rodriguez, J. Bedia, Degradation pathways of emerging contaminants using TiO_2-activated carbon heterostructures in aqueous solution under simulated solar light, Chem. Eng. J. 392 (2020), 124867, https://doi.org/10.1016/J.CEJ.2020.124867.

[37] G. Kresse, J. Furthmüller, Efficient iterative schemes for ab initio total-energy calculations using a plane-wave basis set, Phys. Rev. B 54 (1996) 11169, https://doi.org/10.1103/PhysRevB.54.11169.

[38] J.P. Perdew, J.A. Chevary, S.H. Vosko, K.A. Jackson, M.R. Pederson, D.J. Singh, C. Fiolhais, Atoms, molecules, solids, and surfaces: applications of the generalized gradient approximation for exchange and correlation, Phys. Rev. B. 46 (1992) 6671, https://doi.org/10.1103/PhysRevB.46.6671.

[39] J.P. Perdew, K. Burke, M. Ernzerhof, Generalized gradient approximation made simple, Phys. Rev. Lett. 77 (1996) 3865, https://doi.org/10.1103/PhysRevLett.77.3865.

[40] T. Lu, F. Chen, Multiwfn: a multifunctional wavefunction analyzer, J. Comput. Chem. 33 (2012) 580–592, https://doi.org/10.1002/JCC.22885.

[41] J. Zhang, T. Lu, Efficient evaluation of electrostatic potential with computerized optimized code, Phys. Chem. Chem. Phys. 23 (2021) 20323–20328, https://doi.org/10.1039/D1CP02805G.

[42] W. Humphrey, A. Dalke, K. Schulten, VMD: Visual molecular dynamics, J. Mol. Graph. 14 (1996) 33–38, https://doi.org/10.1016/0263-7855(96)00018-5.

[43] W. Liu, Y. Li, Y. Wang, Y. Zhao, Y. Xu, X. Liu, DFT insights into the degradation mechanism of carbendazim by hydroxyl radicals in aqueous solution, J. Hazard. Mater. 431 (2022), 128577, https://doi.org/10.1016/J.JHAZMAT.2022.128577.

[44] J. Li, Y. Zhao, X. Wang, T. Wang, X. Hou, Rapid microwave synthesis of PCN-134-2D for singlet oxygen based-oxidative degradation of ranitidine under visible light: Mechanism and toxicity assessment, Chem. Eng. J. 443 (2022), 136424, https://doi.org/10.1016/J.CEJ.2022.136424.

[45] United Nations. Globally harmonized systems of classification and labelling of chemicals (GHS). 4th Edition, New York and Genova, 2011.

[46] D. Bůžek, S. Adamec, K. Lang, J. Demel, Metal–organic frameworks vs. buffers: case study of UiO-66 stability, Inorg. Chem. Front. 8 (2021) 720–734, https://doi.org/10.1039/D0QI00973C.

[47] J.H. Cavka, S. Jakobsen, U. Olsbye, N. Guillou, C. Lamberti, S. Bordiga, K. P. Lillerud, A new zirconium inorganic building brick forming metal organic frameworks with exceptional stability, J. Am. Chem. Soc. 130 (2008) 13850–13851, https://doi.org/10.1021/ja8057953.

[48] A. Gómez-Avilés, V. Muelas-Ramos, J. Bedia, J.J. Rodriguez, C. Belver, Thermal post-treatments to enhance the water stability of NH_2-MIL-125(Ti), Catalysts 10 (2020) 603, https://doi.org/10.3390/CATAL10060603.

[49] X. Wang, L. Xie, K.W. Huang, Z. Lai, A rationally designed amino-borane complex in a metal organic framework: a novel reusable hydrogen storage and size-selective reduction material, Chem. Commun. 51 (2015) 7610–7613, https://doi.org/10.1039/C5CC00193E.

[50] C. Sun, L. Karuppasamy, L. Gurusamy, H.J. Yang, C.H. Liu, J. Dong, J.J. Wu, Facile sonochemical synthesis of CdS/COF heterostructured nanocomposites and their enhanced photocatalytic degradation of Bisphenol-A, Sep. Purif. Technol. 271 (2021), 118873, https://doi.org/10.1016/J.SEPPUR.2021.118873.

[51] B. Boruah, R. Gupta, J.M. Modak, G. Madras, Novel insights into the properties of $AgBiO_3$ photocatalyst and its application in immobilized state for 4-nitrophenol degradation and bacteria inactivation, J. Photochem. Photobiol. A Chem. 373 (2019) 105–115, https://doi.org/10.1016/J.JPHOTOCHEM.2018.11.001.

[52] W. Sun, H. Li, H. Li, S. Li, X. Cao, Adsorption mechanisms of ibuprofen and naproxen to UiO-66 and UiO-66-NH_2: Batch experiment and DFT calculation, Chem. Eng. J. 360 (2019) 645–653, https://doi.org/10.1016/J.CEJ.2018.12.021.

[53] Y. Vasseghian, E.N. Dragoi, F. Almomani, V.T. Le, Graphene-based materials for metronidazole degradation: a comprehensive review, Chemosphere 286 (2022), 131727, https://doi.org/10.1016/J.CHEMOSPHERE.2021.131727.

[54] E.M. Kalhori, T.J. Al-Musawi, E. Ghahramani, H. Kazemian, M. Zarrabi, Enhancement of the adsorption capacity of the light-weight expanded clay aggregate surface for the metronidazole antibiotic by coating with MgO nanoparticles: studies on the kinetic, isotherm, and effects of environmental parameters, Chemosphere 175 (2017) 8–20, https://doi.org/10.1016/J.CHEMOSPHERE.2017.02.043.

[55] J. Rivera-Utrilla, G. Prados-Joya, M. Sánchez-Polo, M.A. Ferro-García, I. Bautista-Toledo, Removal of nitroimidazole antibiotics from aqueous solution by adsorption/bioadsorption on activated carbon, J. Hazard. Mater. 170 (2009) 298–305, https://doi.org/10.1016/J.JHAZMAT.2009.04.096.

[56] E. Omrani, A. Ahmadpour, M. Heravi, T.R. Bastami, Novel ZnTi LDH/h-BN nanocomposites for removal of two different organic contaminants: Simultaneous visible light photodegradation of Amaranth and Diazepam, J. Water Process Eng. 47 (2022), 102581, https://doi.org/10.1016/J.JWPE.2022.102581.

[57] W. Wang, J. Yu, Q. Xiang, B. Cheng, Enhanced photocatalytic activity of hierarchical macro/mesoporous TiO_2–graphene composites for photodegradation of acetone in air, Appl. Catal. B Environ. 119 120 (2012) 109–116, https://doi.org/10.1016/J.APCATB.2012.02.035.

[58] M. Li, W. Liu, C. Peng, Q. Ren, W. Lu, W. Deng, A DFT study on reaction of eupatilin with hydroxyl radical in solution, Int. J. Quantum Chem. 113 (2013) 966–974, https://doi.org/10.1002/QUA.24060.

[59] A.R. Lado Ribeiro, N.F.F. Moreira, G. Li Puma, A.M.T. Silva, Impact of water matrix on the removal of micropollutants by advanced oxidation technologies, Chem. Eng. J. 363 (2019) 155–173, https://doi.org/10.1016/J.CEJ.2019.01.080.

[60] C. Chang, H. Yang, L. Kan, W. Mu, Q. Wang, S.Y. Lu, B. Deng, Mechanism and impacts of inorganic ion addition on photocatalytic degradation of triclosan catalyzed by heterostructured $Bi_7O_9I_3$/Bi, J. Taiwan Inst. Chem. Eng. 125 (2021) 176–185, https://doi.org/10.1016/J.JTICE.2021.06.014.

[61] T. Liu, K. Yin, C. Liu, J. Luo, J. Crittenden, W. Zhang, S. Luo, Q. He, Y. Deng, H. Liu, D. Zhang, The role of reactive oxygen species and carbonate radical in oxcarbazepine degradation via UV, UV/H_2O_2: Kinetics, mechanisms and toxicity evaluation, Water Res. 147 (2018) 204–213, https://doi.org/10.1016/J.WATRES.2018.10.007.

[62] M. Peñas-Garzón, M.J. Sampaio, Y.L. Wang, J. Bedia, J.J. Rodriguez, C. Belver, C. G. Silva, J.L. Faria, Solar photocatalytic degradation of parabens using UiO-66-NH_2, Sep. Purif. Technol. 286 (2022), 120467, https://doi.org/10.1016/J.SEPPUR.2022.120467.

[63] E.M. Rodríguez, G. Márquez, M. Tena, P.M. Álvarez, F.J. Beltrán, Determination of main species involved in the first steps of TiO_2 photocatalytic degradation of organics with the use of scavengers: The case of ofloxacin, Appl. Catal. B Environ. 178 (2015) 44–53, https://doi.org/10.1016/J.APCATB.2014.11.002.

[64] R. Sheikhsamany, H. Faghihian, R. Fazaeli, Synthesis of novel HKUST-1-based SnO_2 porous nanocomposite with the photocatalytic capability for degradation of metronidazole, Mater. Sci. Semicond. Process. 138 (2022), 106310, https://doi.org/10.1016/j.mssp.2021.106310.

[65] S. Balasurya, M.K. Okla, A.A. AL-ghamdi, S.A. Al-amri, A.A. Alatar, M.A. Abdel-Maksoud, M. Aufy, S.S. Khan, $CaMoO_4$ modified nanorods-branched Ag_2MoO_4 a nano-diatomic heterojunction as efficient visible-light-driven photocatalysts for water remediation processes and antimicrobial applications, Mater. Today Commun. 34 (2023), 104945, https://doi.org/10.1016/J.MTCOMM.2022.104945.

[66] F. Aoudjit, F. Touahra, L. Aoudjit, O. Cherifi, D. Halliche, Efficient solar heterogeneous photocatalytic degradation of metronidazole using heterojunction semiconductors hybrid nanocomposite, layered double hydroxides, Water Sci. Technol. 82 (2020) 2837–2846, https://doi.org/10.2166/WST.2020.519.

[67] S. Fu, W. Yuan, Y. Yan, H. Liu, X. Shi, F. Zhao, J. Zhou, Highly efficient visible-light photoactivity of Z-scheme MoS_2/Ag_2CO_3 photocatalysts for organic pollutants degradation and bacterial inactivation, J. Environ. Manag. 252 (2019), 109654, https://doi.org/10.1016/J.JENVMAN.2019.109654.

[68] K. Bahareh, M.H. Habibi, High photocatalytic activity of light-driven Fe_2TiO_5 nanoheterostructure toward degradation of antibiotic metronidazole, J. Ind. Eng. Chem. 80 (2019) 292–300, https://doi.org/10.1016/J.JIEC.2019.08.007.

[69] Z.M. Niaki, M. Ghorbani, S.A. Ghoreishi, Synthesis of $ZnFe_2O_4$@UiO-66 nanocomposite for the photocatalytic degradation of metronidazole antibiotic under visible light irradiation, J. Environ. Heal. Sci. Eng. 19 (2021) 1583–1596, https://doi.org/10.1007/S40201-021-00713-X.

[70] J. Cao, J. Li, W. Chu, W. Cen, Facile synthesis of Mn-doped BiOCl for metronidazole photodegradation: optimization, degradation pathway, and mechanism, Chem. Eng. J. 400 (2020), 125813, https://doi.org/10.1016/J.CEJ.2020.125813.

[71] H. Cai, D. Zhang, X. Ma, Z. Ma, A novel ZnO/biochar composite catalysts for visible light degradation of metronidazole, Sep. Purif. Technol. 288 (2022), 120633, https://doi.org/10.1016/J.SEPPUR.2022.120633.
[72] L. Shi, L. Yang, H. Zhang, K. Chang, G. Zhao, T. Kako, J. Ye, Implantation of Iron (III) in porphyrinic metal organic frameworks for highly improved photocatalytic performance, Appl. Catal. B Environ. 224 (2018) 60–68, https://doi.org/10.1016/J.APCATB.2017.10.033.
[73] W.H. Koppenol, D.M. Stanbury, P.L. Bounds, Electrode potentials of partially reduced oxygen species, from dioxygen to water, Free Radic. Biol. Med. 49 (2010) 317–322, https://doi.org/10.1016/J.FREERADBIOMED.2010.04.011.
[74] J. Swathi Padmaja, T.S. Rao, K.V.D. Lakshmi, I.M. Raju, Fabrication of hetero-structured mesoporours TiO_2-$SrTiO_3$ nanocomposite in presence of Gemini surfactant: characterization and application in catalytic degradation of acid orange, J. Environ. Chem. Eng. 6 (2018) 6457–6467, https://doi.org/10.1016/J.JECE.2018.09.016.
[75] A.H. Zyoud, S. Asaad, S.H. Zyoud, S.H. Zyoud, M.H. Helal, N. Qamhieh, A. R. Hajamohideen, H.S. Hilal, Raw clay supported ZnO nanoparticles in photodegradation of 2-chlorophenol under direct solar radiations, J. Environ. Chem. Eng. 8 (2020), 104227, https://doi.org/10.1016/J.JECE.2020.104227.
[76] A.S. Ahmed, T. Ahamad, N. Ahmad, M.Z. Khan, Removal enhancement of acid navy blue dye by GO - TiO_2 nanocomposites synthesized using sonication method, Mater. Chem. Phys. 238 (2019), 121906, https://doi.org/10.1016/J.MATCHEMPHYS.2019.121906.
[77] X.H. Yi, H. Ji, C.C. Wang, Y. Li, Y.H. Li, C. Zhao, A. Wang, H. Fu, P. Wang, X. Zhao, W. Liu, Photocatalysis-activated SR-AOP over PDINH/MIL-88A(Fe) composites for boosted chloroquine phosphate degradation: Performance, mechanism, pathway and DFT calculations, Appl. Catal. B Environ. 293 (2021), 120229, https://doi.org/10.1016/J.APCATB.2021.120229.
[78] Q. Su, J. Li, B. Wang, Y. Li, Direct Z-scheme Bi_2MoO_6/ UiO-66-NH_2 heterojunctions for enhanced photocatalytic degradation of ofloxacin and ciprofloxacin under visible light, Appl. Catal. B: Environ. 318 (2022), 121820, https://doi.org/10.1016/j.apcatb.2022.121820.
[79] Y. Wu, H. Ji, Q. Liu, Z. Sun, P. Li, P. Ding, M. Guo, X. Yi, W. Xu, C.C. Wang, S. Gao, Q. Wang, W. Liu, S. Chen, Visible light photocatalytic degradation of sulfanilamide enhanced by Mo doping of BiOBr nanoflowers, J. Hazard. Mater. 424 (2022), 127563, https://doi.org/10.1016/J.JHAZMAT.2021.127563.
[80] X. Gao, J. Chen, H. Che, Y. Ao, P. Wang, Rationally constructing of a novel composite photocatalyst with multi charge transfer channels for highly efficient sulfamethoxazole elimination: mechanism, degradation pathway and DFT calculation, Chem. Eng. J. 426 (2021), 131585, https://doi.org/10.1016/J.CEJ.2021.131585.
[81] J. Li, J. Chen, Y. Ao, X. Gao, H. Che, P. Wang, Prominent dual Z-scheme mechanism on phase junction WO_3/CdS for enhanced visible-light-responsive photocatalytic performance on imidacloprid degradation, Sep. Purif. Technol. 281 (2022), 119863, https://doi.org/10.1016/J.SEPPUR.2021.119863.
[82] H. Abbasi-Asl, M.M. Sabzehmeidani, M. Ghaedi, Efficient degradation of metronidazole antibiotic by TiO_2/Ag_3PO_4/g–C_3N_4 ternary composite photocatalyst in a continuous flow-loop photoreactor, J. Environ. Chem. Eng. 9 (2021), 105963, https://doi.org/10.1016/J.JECE.2021.105963.
[83] J. Cao, J. Li, W. Chu, W. Cen, Facile synthesis of Mn-doped BiOCl for metronidazole photodegradation: optimization, degradation pathway, and mechanism, Chem. Eng. J. 400 (2020), 125813, https://doi.org/10.1016/J.CEJ.2020.125813.
[84] J. Sun, Y. Hou, Z. Yu, L. Tu, Y. Yan, S. Qin, S. Chen, D. Lan, H. Zhu, S. Wang, Visible-light-driven Z-scheme $Zn_3In_2S_6$/AgBr photocatalyst for boosting simultaneous Cr(VI) reduction and metronidazole oxidation: kinetics, degradation pathways and mechanism, J. Hazard. Mater. 419 (2021), 126543, https://doi.org/10.1016/J.JHAZMAT.2021.126543.
[85] Z. Li, S. Chen, Z. Li, J. Sun, J. Yang, J. Wei, S. Wang, H. Song, Y. Hou, Visible light driven antibiotics degradation using S-scheme Bi_2WO_6/$CoIn_2S_4$ heterojunction: Mechanism, degradation pathways and toxicity assessment, Chemosphere 303 (2022), 135113, https://doi.org/10.1016/J.CHEMOSPHERE.2022.135113.
[86] B. Harikumar, S.Sudheer Khan, Hierarchical construction of ZrO_2/$CaCr_2O_4$/$BiOIO_3$ ternary photocatalyst: Photodegradation of antibiotics, degradation pathway, toxicity assessment, and genotoxicity studies, Chem. Eng. J. 442 (2022), 136107, https://doi.org/10.1016/J.CEJ.2022.136107.